HAL open science

# Ion implantation effects on the microstructure, electrical resistivity and thermal conductivity of amorphous CrSi2 thin films

M. Timm, E. Oliviero, W. Sun, Séverine Gomès, Georges Hamaoui, P. Fichtner, N. Frety

## To cite this version:

M. Timm, E. Oliviero, W. Sun, Séverine Gomès, Georges Hamaoui, et al.. Ion implantation effects on the microstructure, electrical resistivity and thermal conductivity of amorphous CrSi2 thin films. Journal of Materials Science, 2022, 57 (2), pp.1174-1185. 10.1007/s10853-021-06674-8 . hal-03799435

**HAL Id: hal-03799435**

**https://hal.science/hal-03799435v1**

Submitted on 21 Mar 2023

**HAL** is a multi-disciplinary open access archive for the deposit and dissemination of scientific research documents, whether they are published or not. The documents may come from teaching and research institutions in France or abroad, or from public or private research centers.

L'archive ouverte pluridisciplinaire **HAL**, est destinée au dépôt et à la diffusion de documents scientifiques de niveau recherche, publiés ou non, émanant des établissements d'enseignement et de recherche français ou étrangers, des laboratoires publics ou privés.

Distributed under a Creative Commons Attribution 4.0 International License

# Ion implantation effects on the microstructure, electrical resistivity and thermal conductivity of amorphous $CrSi_2$ thin films

M. M. Timm[1,7,*], E. Oliviero[2,3], W. Sun[4], S. Gomes[4], G. Hamaoui[5], P. F. P. Fichtner[1,6], and N. Frety[2,*]

[1] *Instituto de Física, Universidade Federal Do Rio Grande Do Sul, Porto Alegre, RS, Brazil*
[2] *ICGM, CNRS, Univ. Montpellier, Montpellier, France*
[3] *MEA, CNRS, Univ. Montpellier, Montpellier, France*
[4] *CNRS, INSA Lyon, CETHIL, Univ Lyon, UMR5008, 69621 Villeurbanne, France*
[5] *ESYCOM Laboratory, CNRS, Université Gustave Eiffel, 77454 Marne-la-Vallée, France*
[6] *Escola de Engenharia, Universidade Federal Do Rio Grande Do Sul, Porto Alegre, RS, Brazil*
[7] *Present address: INSA, UCBL, CNRS, MATEIS, Univ-Lyon, UMR 5510, 69621 Villeurbanne, France*

## ABSTRACT

The microstructural changes induced by ion implantation may lead to advantageous modifications of chromium disilicide's ($CrSi_2$) electrical and thermal properties. As a potential thermoelectric material, $CrSi_2$ has attracted attention due to its semiconductor properties and high thermal stability. This contribution investigates the influence of different ion species and implantation conditions on the microstructure, electrical resistivity $\rho$ and thermal conductivity $\kappa$ behaviors in amorphous $CrSi_2$ thin films. $\sim$ 260-nm-thick $CrSi_2$ films were produced by magnetron sputtering and deposited onto a $SiO_2$/Si substrate. Samples were implanted at room temperature either with Ne or Al ions to form a concentration–depth plateau reaching a concentration of $\approx$ 1.0 at.% (Ne), or $\approx$ 0.008 at.% (Al). Ne and Al implantations were also performed with the targets heated at 250 °C. The microstructural modifications were characterized via TEM and STEM-EDX. The electrical resistivity $\rho$ was measured by the van der Pauw method, and the thermal conductivity $\kappa$ measurements were obtained with SThM. The results obtained show that room temperature Al and Ne implantations cause the reduction of $\rho$ as compared to the pristine film. In contrast, the $\rho$ values are significantly higher for Ne and Al implantations in heated substrates. The microstructure evolution, electrical and thermal behaviors are discussed considering the effects of radiation damage and the formation of dense nanocrystallite arrays during the implantation process.

## Introduction

Transition metal silicides ($TMSi_2$) have favorable physical properties that make them suitable for applications in microelectronics [1], ceramics [2], spintronic [3] and thermoelectricity [4, 5]. Among them, $CrSi_2$ is a narrow bandgap p-type semiconductor with a high electrical conductivity considered for a wide range of applications, from electro-optic interconnects [6], Schottky junctions [7, 8], to IR detection devices [9, 10]. Furthermore, $CrSi_2$ is chemically and thermally stable at high temperatures. Combined with its high electrical conductivity and Seebeck coefficient, $CrSi_2$ becomes an engaging material for potential use in thermoelectric applications [11–14]. However, $CrSi_2$ has a high thermal conductivity, which negatively affects the figure of merit ZT and hinders its use as practical thermoelectric devices [11, 15]. Nevertheless, due to its extensive range of potential applications, it is of great interest to understand the behavior of $CrSi_2$ under different conditions.

Many studies have been performed in single and polycrystalline $CrSi_2$, including bulk and thin films. It has been shown, for example, that the electrical properties of $CrSi_2$ are pretty sensitive to variations in the composite stoichiometry [16], deposition methods [17, 18], thermal treatments [19] and the nature of the substrate [20, 21]. Most studies have focused on crystalline $CrSi_2$, but in its amorphous form, $CrSi_2$ can also present interesting behaviors. Amorphous materials have a wide range of applications in microelectronics devices, such as thin-film transistors (TFTs) [22], memristors [23], solid-state nonvolatile phase-change memory (PCM) [24] and photovoltaic solar cells [25], and in thermoelectric (TE) devices [26]. It has been suggested that some amorphous semiconductors can attain good thermoelectric properties due to their modest to good electrical conductivity ($\sigma$) and poor thermal conductivity ($\kappa$), improving the $\sigma/\kappa$ ratio as required by the energy conversion figure of merit [26–28]. The performance of these devices depends on the operating temperature, also concerning their physical properties and thermal stability. This situation is challenging for amorphous structures and of great importance to optimize their use concerning device functionality and reliability.

In this sense, we explore the use of ion implantation to modify the electrical and thermal properties of amorphous $CrSi_2$. The combination of ion implantation and *in situ* or *ex situ* thermal treatments allows tailoring several properties of semiconductors. It includes not only the electrical conductivity [29–31] but also the microstructure configuration to provide, for example, impurity gettering [32, 33], end-of-range defect engineering [34] or even strain relaxation effects [35, 36]. Ion beam modification techniques are explored to improve crystalline materials' electric and thermal properties via doping or by forming point and extended defects to act as phonon scattering centers, thus reducing the phonon contribution to the thermal conductivity. For amorphous materials, the situation is different. Ion implantation can still be used for doping, but the microstructure modification requires a different approach. Amorphous materials provide an extra degree of freedom concerning ion implantation experiments. Since the ion implantation/irradiation processes can occur at nonthermal equilibrium conditions, it allows modifying the compaction degree of the amorphous lattices or enables the formation of crystalline clusters and even the promotion of complete recrystallization resulting in a highly defective crystal lattice.

In this paper, we report on the effects of Ne and Al ion implantation on the microstructure, electrical and thermal properties of amorphous $CrSi_2$ thin films. The implantations are done at different fluences in substrates kept at room temperature or heated at 250 °C. The microstructure of the samples is characterized by transmission electron microscopy (TEM). We also use electrical resistivity and scanning thermal microscopy (SThM) measurements to assess electrical and thermal conductivities. The discussions consider Ne as an inert element and how the matrix responds to the implantation-induced atomic displacements, causing, for example, the formation of nanosized Ne bubbles and $CrSi_2$ crystallites. Al is a common dopant in crystalline $CrSi_2$. Here we investigate its doping and irradiation effects throughout the amorphous $CrSi_2$ films. The results obtained demonstrate that the ion implantation/irradiation process causes significant modifications to the electrical and thermal properties of amorphous $CrSi_2$ thin films.

## Experimental procedure

$CrSi_2$ amorphous films with an average thickness of 260 nm were deposited in Si (100) substrates by radio-frequency magnetron sputtering technique in a high-vacuum chamber (base pressure of $2 \times 10^{-6}$ mbar) with a high-purity $CrSi_2$ target (3", 99.95%, Neyco) using the experimental protocol developed previously [37]. The sputtering targets were operated at 120 W under a pressure of 0.51 Pa with a high-purity Ar flow (99.99%). A $SiO_2$ sublayer with a thickness of 25 nm was deposited by sputtering before the $CrSi_2$ layer. The depositions were done at room temperature with the multi-target Plassys MP4505 equipment (CTM, Université de Montpellier, France). One series of samples contains Al implantations at distinct energies, calculated to produce a uniform concentration–depth distribution along the film. A second sample series has Ne implantations in a uniform concentration–depth distribution. The Ne and Al implantations were done at room temperature and at a temperature of 250 °C. The fluences of the Ne and Al implantations at 250 °C were adjusted to produce similar damage levels, computed in displacement per atom (dpa) units [38]. The implantation profiles and fluences, simulated using the SRIM code ($E_d = 25$ eV (Cr), $E_d = 15$ eV (Si)) [39], lead to atomic concentrations of $\approx$ 0.008 at.% for Al (room temperature implantation), of $\approx$ 0.64 at.% for Al (250 °C implantation) and $\approx$ 1 at.% for Ne. All the implantation experiments were done using a 500 kV HVEE ion implanter (Laboratório de Implantação Iônica, Instituto de Física, UFRGS, Brazil) maintaining the beam current below 500 nA/cm$^2$ to avoid the heating of the substrate that could affect the sample microstructure. The sample's temperature during implantations is kept constant, feedback-controlled using a type K thermocouple and a Tantalum resistance attached to the sample holder. Table 1 summarizes the implantation parameters.

The composition and stoichiometry of the as-deposited $CrSi_2$ film were accessed via Rutherford backscattering spectrometry (RBS). The RBS measurements were performed using a 1.5 MeV $He^+$ beam from a 3 MeV HVEE Tandem accelerator (Laboratório de Implantação Iônica, Instituto de Física, UFRGS, Brazil). The microstructure evolution of the samples was analyzed via transmission electron microscopy (TEM) using cross-sectional samples prepared by focused ion beam (FIB) with the FEI Strata DB 235 equipment (IEMN, Lille, France). TEM observations were made using a JEOL JEM 2200FS transmission electron microscope operating at 200 kV (MEA Platform, Université de Montpellier, France). Ne and Al distributions along the $CrSi_2$ film were assessed via scanning transmission electron microscopy–energy-dispersive X-ray spectrometry (STEM-EDX). The STEM-EDX measurements were performed using a 100 mm$^2$ Oxford Xmax TLE windowless detector. The crystallinity of the $CrSi_2$ samples considered in this study was assessed via the selected area electron diffraction (SAED) technique. The electrical resistivity ($\rho$) measurements on implanted and non-implanted $CrSi_2$ thin layers were carried out between 80 and 330 K with a magnetic field of 0.5 T by the van der Pauw method. The electric contacts were made using In droplets, and the measurements were performed with an Ecopia HMS 5000 four-point probe equipment (CTM, Université de Montpellier, France). Scanning thermal microscopy (SThM) in active mode using the Wollaston wire probe [40] in ambient air conditions was used to characterize the thermal conductivity ($\kappa$) dependence of the $CrSi_2$ films.

## Results and discussion

### As-deposited sample characterization

Figure 1a shows cross-sectional TEM micrographs of the as-deposited, non-implanted $CrSi_2$ sample. The film was deposited over a Si wafer containing a 25 nm $SiO_2$ layer. The S arrow points to the surface of the film. For the FIB sample preparation, the film was covered by a thin carbon layer and then by a Pt film also appearing in the micrograph. The $CrSi_2$ film deposition process results in columnar structures due to the low mobility of the atoms adsorbed by the substrate surface during the sputtering deposition process. This type of growth is predicted for room temperature depositions by the Thornton model in zone 1 [41, 42]. Figure 1b shows the SAED pattern from the $CrSi_2$ film depicted in Fig. 1a. In cross-sectional TEM specimens, SAED measurements are sensitive to the formation of small crystallites with characteristic dimensions above 1 nm. The observation of a diffuse and broad ring pattern indicates that the sample can be considered amorphous within the sensitivity level of the technique. Figure 1c depicts

**Table 1** Ion implantation parameters

| Ne | | Al | | | |
|---|---|---|---|---|---|
| Room temperature and T = 250 °C | | Room temperature | | T = 250 °C | |
| Energy (keV) | Fluence (at/cm$^2$) | Energy (keV) | Fluence (at/cm$^2$) | Energy (keV) | Fluence (at/cm$^2$) |
| 250 | $1 \times 10^{16}$ | 200 | $1 \times 10^{14}$ | 200 | $8 \times 10^{15}$ |
| 120 | $7 \times 10^{15}$ | 90 | $4.5 \times 10^{13}$ | 90 | $3.6 \times 10^{15}$ |
| 50 | $4 \times 10^{15}$ | 40 | $1 \times 10^{13}$ | 40 | $8 \times 10^{14}$ |
| 20 | $1.5 \times 10^{15}$ | 30 | $1 \times 10^{13}$ | 30 | $8 \times 10^{14}$ |
| Concentration (at.%) | | | | | |
| ~ 1.0 | | ~ 0.008 | | ~ 0.64 | |

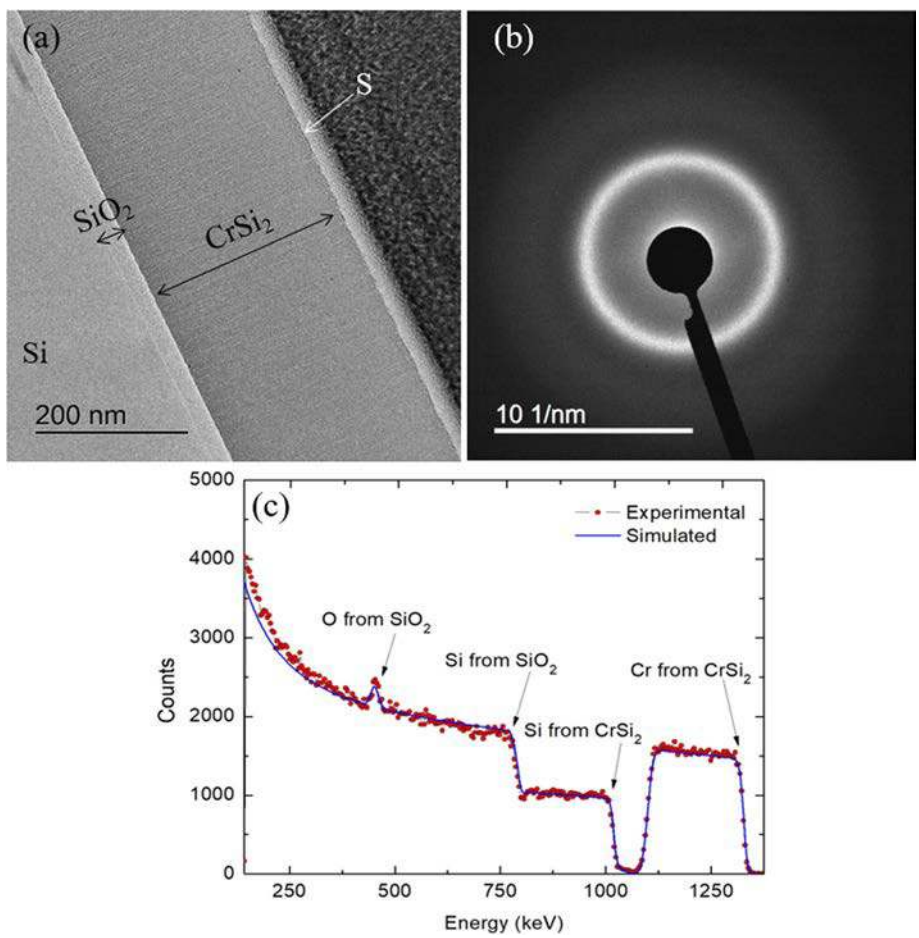


**Figure 1** **a** Cross-sectional TEM micrograph showing the as-deposited $CrSi_2$ thin film, where the S vector points to the surface of the film. The Si substrate and the $SiO_2$ layer are also indicated in the image. **b** Selected area electron diffraction (SAED) pattern of the as-deposited $CrSi_2$ sample shown in (a). **c** RBS spectrum of the as-deposited $CrSi_2$ film.

the RBS spectrum. It is well fitted by a SIMNRA code [43] simulation (continuous line), demonstrating that the $CrSi_2$ film is stoichiometric.

## Implantations at room temperature

Figure 2a, b shows cross-sectional TEM micrographs of room temperature (RT) Ne- and Al-implanted $CrSi_2$ samples. The Ne implantation to a concentration of $\approx$1 at.% triggered the formation of a dense array of Ne-filled cavities (i.e., bubbles) distributed

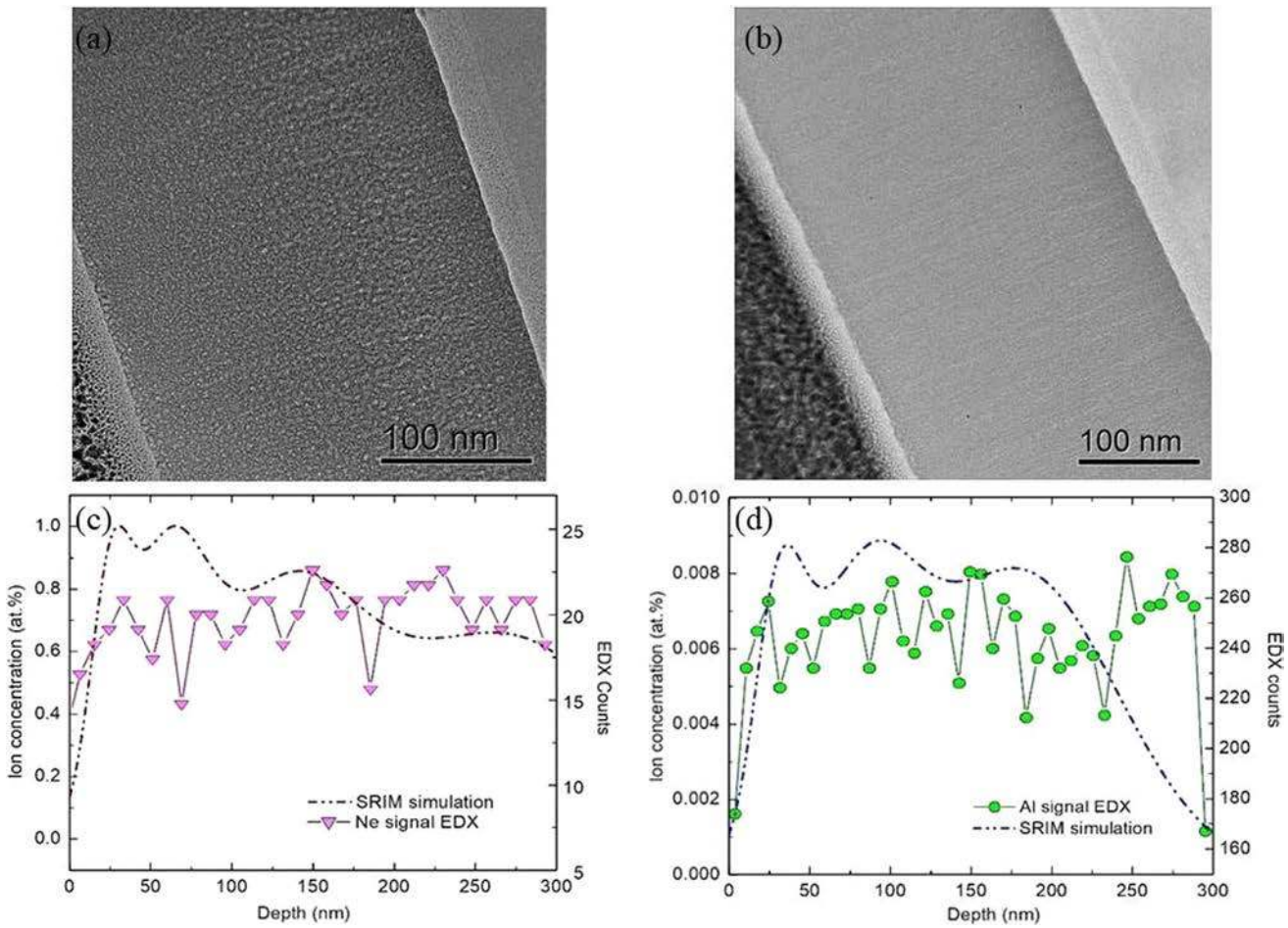


**Figure 2** Cross-sectional TEM micrograph for the $CrSi_2$ sample implanted at room temperature with **a** Ne and **b** Al. EDX spectrum appears superimposed with SRIM ion concentration–depth profile simulation for **c** Ne and **d** Al implantation.

throughout the film (white disks surrounded by a dark ring produced by bright-field underfocus imaging conditions). Figure 2a shows that Ne bubble formation preferentially occurs along with the columnar structures of the film. The Al implantation to a concentration of $\approx$ 0.008 at.% (Fig. 2b) does not affect the columnar structure arrangement. Also, it does not cause any other observable microstructure modification concerning the pristine structure shown in Fig. 1a.

The scattered points in Fig. 2c, d represent, respectively, the EDX signals for Ne and Al as a function of distance along with the film. The dash dotted lines correspond to the Ne and Al concentration–depth profiles predicted by SRIM simulations [39]. The EDX measurements indicate that the concentration–depth profile of the implanted Ne ions did not diffuse much into the $CrSi_2$ layer due to the trapping of Ne by bubbles. Differently, Al has diffused along the film due to implantation-enhanced diffusion and knock-on by successive ions. The corresponding SAED patterns of Ne- and Al-implanted samples (not shown) remain similar to the one in Fig. 1b. These measurements indicate that the RT implantations preserved the amorphous structure of the film.

Inert gases have an extremely low solubility limit and tend to agglomerate into more stable gas–vacancy complexes leading to bubble formation [44–46]. The same behavior also occurs in amorphous structures where the concept of vacancies correlates with small free volume pockets in the network structure [47]. The resolution limit for underfocus phase-contrast imaging conditions in TEM observations is about 0.7 nm. Therefore, Fig. 2a reveals only the visible bubbles, coarsened by gettering additional Ne atoms or by interacting with other surrounding bubbles via, for example, irradiation-induced bubble

migration and coalescence process [45]. The same atomic mobility behavior discussed for the Ne atoms may also occur for the Al-implanted sample. In this case, the atomic mobility can be inferred by the difference in the Al concentration–depth profile measured by EDX and predicted by the SRIM code (Fig. 2d).

## Ne Implantation at 250 °C

The effects of the Ne implantation at 250 °C in the $CrSi_2$ film structure can be inferred by the TEM micrographs presented in Fig. 3a which shows that the implantation effects are quite similar within the entire film thickness.

Figure 3b shows an enlarged micrograph from a region of Fig. 3a. This figure better illustrates the presence of crystal grains (darker domains obtained via bright-field diffraction contrast) and the homogeneously dispersed Ne bubbles (depicted in bright-field underfocus imaging conditions). The micrograph also suggests that the columnar grain structure has been smoothed out. These features are quite distinct from those observed for the RT implantation case (Fig. 2a). Figure 3c shows the EDX measurement for Ne distribution as a function of distance in the film. The depth distribution of the Ne content is very similar to the one obtained by implantation at room temperature (Fig. 2c).

Figure 3a, b shows that, for implantations at 250 °C, a significant fraction of the amorphous structure has been transformed into randomly oriented crystallites with sizes with diameters from 5 to about 20 nm. This phenomenon is also evidenced by the dense ringlike distribution of diffraction spots in the SAED pattern presented in Fig. 4a. The ring pattern is well fitted using the hexagonal structure of the $CrSi_2$ crystal lattice (space group $P6_222$, lattice parameters $a$ = 4.42758 Å and $c$ = 6.36805 Å, Wyckoff positions *3d* (Cr) and *6j* (Si)) [12]. The (h,k,l) index of the rings is presented in the figure. Additional rings formed by rather weak spots are observed, showing that other phases have been produced in a minor volume fraction. Figure 4b shows a dark-field TEM micrograph produced by selecting a spot from the innermost ring of the SAED pattern. The dark-field micrograph was taken in the same region as the bright-field ones from Figs. 4a, b.

It seems worth noting that the Ne implantation at 250 °C induced local crystallization reactions at a temperature about eighty degrees lower than the crystallization temperature T = 327 °C expected by thermal treatments [48]. This phenomenon is typically expected in ion-implanted/irradiated samples and is usually interpreted as a radiation-enhanced phase transformation process [49]. The formation of a dense array of nanocrystallites is probably connected to the bubbles and the remaining columnar grain boundaries, which may act as inhomogeneous nucleation sites for the amorphous–crystalline phase transition.

## Electrical resistivity measurements

Figure 5 shows the electrical resistivity ρ measurements as a function of temperature T for the as-deposited and implanted samples. The behavior of the ρ(T) curve for the as-deposited sample is in good agreement with previous measurements in CrSi2 [12, 50]. The ρ(T) curves for the RT Ne and Al

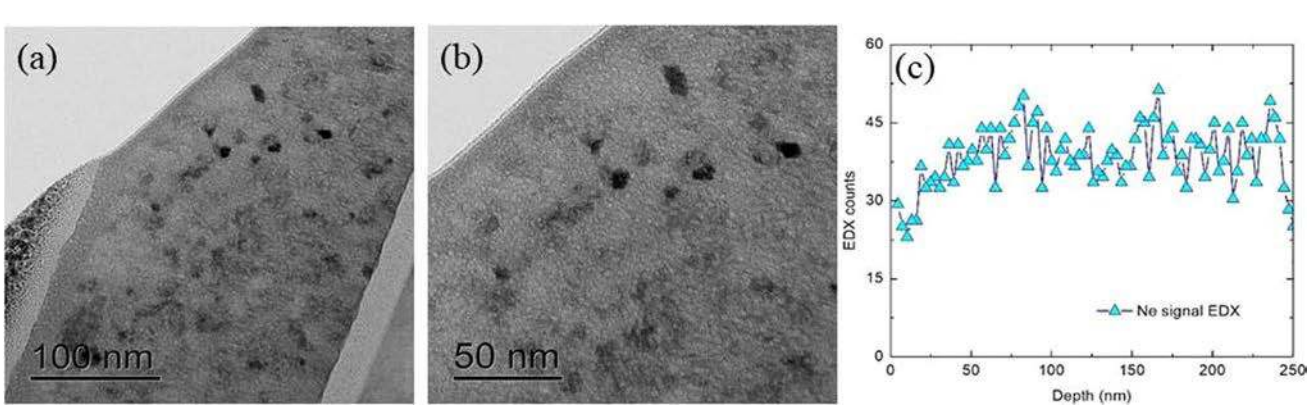


**Figure 3** **a** Cross-sectional TEM micrographs of the $CrSi_2$ sample implanted with Ne at 250 °C; **b** same sample at a higher magnification; and **c** Ne EDX profile as a function of distance in the film.

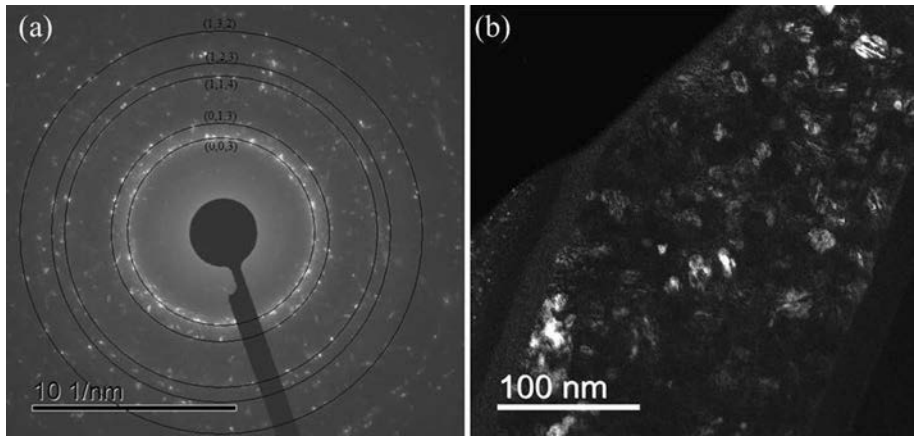


**Figure 4** **a** SAED pattern superimposed with the theoretical planes of crystalline $CrSi_2$. **b** Dark-field contrast micrograph from the same area shown in Fig. 3a of the $CrSi_2$ sample implanted with Ne at 250 °C.

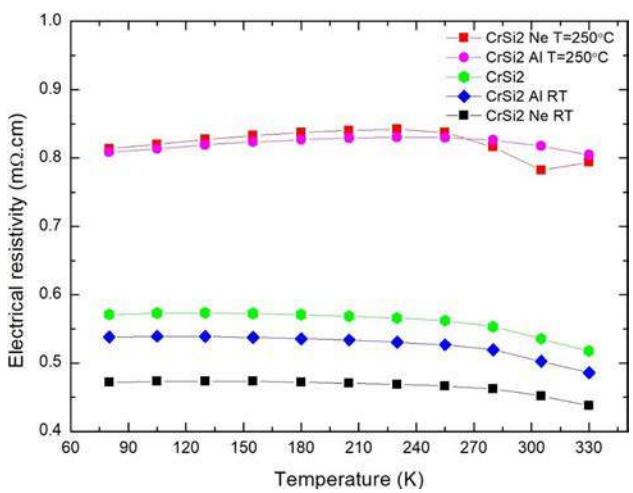


**Figure 5** Electrical resistivity ρ measurements as a function of the temperature of as-deposited and implanted $CrSi_2$ samples. The lines serve as a guide for the eyes. Measurements error bars are within the symbol size.

implantations present a shift toward lower ρ values. The curves show similar temperature dependence to the pristine deposited film for the measured temperature range from 60 to 330 K.

Al atoms can be considered as acceptor dopants for $CrSi_2$ [50]. If these atoms become active dopants within the amorphous lattice, a charge carrier concentration is expected to increase within the valence band and, therefore, decrease film resistivity. This behavior is indeed in qualitative agreement with our experimental results. On the other side, as an inert gas atom, Ne should not behave as a dopant. Nevertheless, the decrease in ρ values is more pronounced for the Ne than for the Al implantation case. This behavior seems consistent with the concept that small defect clusters may become electrically active and cause the formation of charge carriers as observed for crystalline semiconducting lattices. This argument has been previously presented, for example, by Saji et al., that report a decrease in ρ observed in $Bi_2Se_3$ samples after H and He irradiation [51]. Bala et al. also consider that the reduction in ρ for Ag-implanted PbTe samples is caused by electrically active defects produced during ion implantation [52]. They also show that the decrease in ρ depends on the implantation fluence, which correlates with the buildup of the defect concentration.

Furthermore, Banwell et al. performed Ne, Ar and Xe irradiations in $CrSi_2$ and obtained a considerable decrease in ρ [53]. They also explained the result in terms of an increase in free carrier concentration that arises from completely ionized defects produced by the irradiation. As presented in [54] and [55], the concept of implantation-induced defects affecting the carrier concentration in crystals can also be generalized to an amorphous lattice considering the formation of dangling bonds. We can use the same arguments to explain the resistivity reduction observed for both the Ne and the Al implantation cases. Since the damage level for the RT Al implantation is approximately 100 times lower than the Ne implantation, the corresponding resistivity decrease seems to be more affected by the Al doping effect. On the other side, the dangling bonds produced by the RT Ne implantation reduce the resistivity despite the bubble system effect. However, if the defects produced by ion implantation/irradiation processes do not affect the carrier concentration, the opposite behavior can be expected. For example, in a recent study, Tureson et al. have analyzed the influence of room temperature Mg implantation on the thermoelectric properties of ScN films [56]. They observed

an increase in ρ and a decrease in κ. The increase in ρ was explained considering that the defects induced by the implantation process contribute to scattering the charge carriers, causing a significant reduction in their mobility. However, in the case of amorphous lattices, atomic displacements induced by ion implantation may not produce lattice defects acting as efficient scattering centers for charge carriers.

The electrical resistivity values for the Ne implantation at 250 °C are about 70% larger than the as-deposited film value (Fig. 5). Figure 4 shows that the Ne implantation causes the formation of a dense array of randomly oriented nanocrystalline structures. These nanocrystallites introduce interfaces that can selectively scatter carriers. The increase in electrical resistivity in partially crystallized $CrSi_2$ thin films was also observed by Moll et al. [57]. Its occurrence is also credited to an additional interface scattering mechanism produced by the presence of nanocrystallites. We must also consider that the implantation temperature increases the mobility of defects produced by Ne ions and can induce their agglomeration. These defects can reduce the charge carrier mean free path with a consequent increase in electrical resistivity. In addition, considering that, if the average size of the nanocrystals is comparable to the de Broglie wavelength of the carriers in the material, the crystallite may effectively act as scattering centers [58]. For $CrSi_2$ samples, the de Broglie wavelength is $\lambda = 5$ nm, comparable to the average crystallite size produced by the 250 °C Ne implantation. In the present case, we assume, however, that it is the lattice disorder generated by a high number of nanocrystallites' interface regions the main cause for the increase in electrical resistivity. The same explanation applies to the Al 250 °C case, which presents similar electric resistivity values (Fig. 5).

## Thermal conductivity measurements

Figure 6 shows the effective thermal conductivity ($\kappa_{eff}$) measurements obtained with SThM for the ion-implanted samples. $\kappa_{eff}$ could not be successfully determined for the as-deposited sample because the SThM technique presents significant uncertainties with increasing thermal conductivity values. Therefore, following the results from Ref. [12], we assume $\kappa_{eff} \approx 10$ W/mK as a reference value for the as-deposited film. For each sample, ten point measurements were taken at five different locations. The

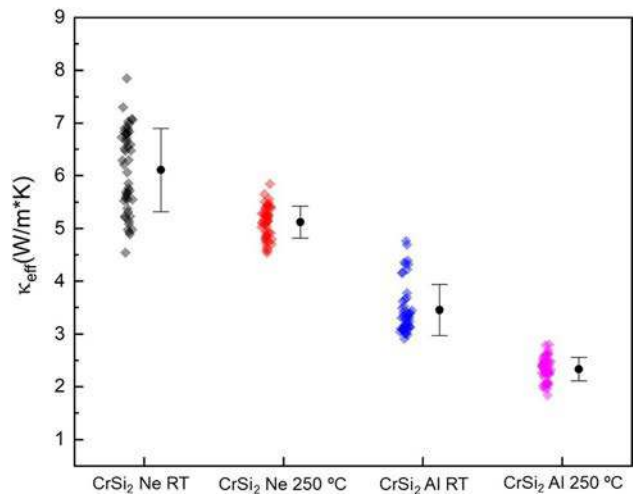


**Figure 6** Thermal conductivity measurements of the implanted $CrSi_2$ samples. The error bars represent the standard deviation of the measurements, and the solid black circle represents the mean $\kappa_{eff}$ value of each sample.

effective thermal conductivity of thin films and layered compounds may be considered a logical extension of the thermal conductivity, such as for solid, liquid or gaseous materials [59]. In our case, the effective thermal conductivity $\kappa_{eff}$ is the thermal conductivity of the film-on-substrate system (not just $CrSi_2$); its value includes a contribution from the 25 nm $SiO_2$ film, that from the Si substrate and the thermal contact resistances between the layers.

When compared to the as-deposited sample ($\kappa_{eff} \approx 10$ W/mK) [12], all the implanted samples present a significant decrease in the thermal conductivity. The samples implanted at RT present a less pronounced reduction in thermal conductivity than their 250 °C counterparts. In the case of the Al implantation at RT, even though the implanted atomic concentration is very low compared to Ne at RT (see Table 1), the formation of defect clusters can play a dominant role in controlling thermal conductivity behavior. It has been shown, for example, that even very low irradiation doses (as low as 0.00032 dpa–displacement per atom) decrease the thermal diffusivity of self-irradiated tungsten due to the formation of sub-nanometric defects [60]. Furthermore, the introduction of isoelectronic elements preserves the crystalline electronic structure while enhancing electrical conductivity and creating a mass contrast that disrupts the path of the heat carriers [48, 61]. In this sense, Perumal et al. showed that the introduction of Al and Mn as co-substitutors in $CrSi_2$ induces

a decrease in thermal conductivity due to a mass fluctuation effect from the atomic weight difference between the solute and solvent atoms [50].

In the case of the samples implanted with Ne, the critical feature is the presence of Ne bubbles. Bubbles represent a discontinuity on the solid structure of the matrix and may act as efficient scattering centers for the phonons. Therefore, the phononic component of the thermal conductivity decreases, explaining the reduction observed on the $\kappa_{eff}$ measurements of these two samples compared to the non-implanted $CrSi_2$ sample. The samples implanted with Ne and Al at a temperature of 250 °C present a more significant reduction in $\kappa_{eff}$ than the RT Ne- and Al-implanted samples. In these cases, we can assume that the nanocrystallites formed during the 250 °C implantations are effective scattering centers for the phonons and contribute to a more pronounced effect on $\kappa_{eff}$. Similarly, Novikov et al. show that nanocrystal interfaces in stoichiometric $CrSi_2$ thin films largely contribute to the increase in the electrical resistivity, which also happens in our case for the 250 °C Ne-implanted $CrSi_2$ sample (see Fig. 5) but also to the decrease in the thermal conductivity [58]. For the Al 250 °C case, the combination of the nanocrystallites and the mass fluctuation effect discussed above could explain the significant decrease in the thermal conductivity.

## Conclusions

This paper shows that ion implantation induces substantial modifications on the microstructure, electrical resistivity ρ and thermal conductivity κ of amorphous 260-nm-thick $CrSi_2$ films. Al and Ne implantations performed at room temperature induce a decrease in both ρ and κ. The decrease of ρ is attributed to the introduction of dopants (Al) or of electrically active irradiation-induced defects acting as dopants. The decrease in κ results from the formation of Ne bubbles acting as scattering centers for phonons or by creating a mass contrast effect by incorporating Al in the amorphous matrix. We also demonstrate the increase in ρ for Ne and Al implantations at 250 °C. This is attributed to the formation of a dense array of nanocrystallites that interfere on the mobility of charge carriers. The presence of such a dense array of nanocrystallites also causes the decrease of κ.

In a more general way, this work demonstrates that electrical and thermal conductivity behavior of amorphous structures can be tailored via ion implantation or irradiation techniques. This is done by exploring doping, amorphous to crystalline phase transitions and irradiation-induced electrically active defects, providing new possibilities for applications.

## Acknowledgements

The authors would like to acknowledge the use of the facilities from the Laboratório de Implantação Iônica—UFRGS, from the Plateforme MEA—Université de Montpellier and from the Centrale de Technologie en Micro et nanoélectronique (CTM)—Université de Montpellier. They also thank D. Troadec (IENM, Lille, France) for the FIB sample preparation. This study was partially financed by Conselho Nacional de Desenvolvimento Científico e Tecnológico—Brazil (CNPq), by the Coordenação de Aperfeiçoamento de Pessoal de Nível Superior—Brazil (CAPES)—Finance Code 001 and partially supported by the French RENATECH network and the Chinese Scholarship Council (CSC). The authors declare no conflict of interest or competing interests.

## References

[1] Murarka SP (1995) Silicide thin films and their applications in microelectronics. Intermetallics 3:173–186

[2] Chen X, Liang C (2019) Transition metal silicides: fundamentals, preparation and catalytic applications. Catal Sci Technol 9:4785–4820. https://doi.org/10.1039/c9cy00533a

[3] Jin S, Schmitt AL, Zhu L et al (2006) Synthesis, Characterization and Physical Properties of Transition Metal Silicide Nanowires. Proc SPIE 6370. Nanomater Synth Integr Sensors, Electron Photonics, Electro-Optics 63700O:1–10. https://doi.org/10.1117/12.687206

[4] Fedorov MI, Zaitsev VK (2009) Thermoelectrics of transition metal silicides. In: Rowe DM (ed) Thermoelectrics Handbook: macro to nano. CRC Press

[5] Nozariasbmarz A, Agarwal A, Coutant ZA et al (2017) Thermoelectric silicides A review. Jpn J Appl Phys 56:05DA04. https://doi.org/10.7567/JJAP.56.05DA04

[6] Bost MC, Mahan JE (1986) Semiconducting silicides as potential materials for electro-optic very large scale integrated circuit interconnects. J Vac Sci Technol B 4:1336–1338. https://doi.org/10.1116/1.583454

[7] Barus M, Donoval D (1993) Analysis of I-V measurements on CrSi2-Si Schottky structures in a wide temperature range. Solid State Electron 36:969–974

[8] Anilturk OS, Turan R (2000) Electrical transport at a non-ideal CrSi2-Si junction. Solid State Electron 44:41–48

[9] Bost MC, Mahan JE, S MCB, Mahan JE, (1988) An investigation of the optical constants and band gap of chromium disilicide. J Appl Phys 63:839–844. https://doi.org/10.1063/1.340078

[10] Goroshko D, Chusovitin E, Shevlyagin A et al (2013) Enhancement of near IR ensitivity of silicon-based photodetectors. Phys Status Solidi C 10:1844–1846. https://doi.org/10.1002/pssc.201300402

[11] Abd El Qader M, Venkat R, Kumar R et al (2013) Structural, electrical, and thermoelectric properties of CrSi2 thin films. Thin Solid Films 545:100–105. https://doi.org/10.1016/j.tsf.2013.07.040

[12] Dasgupta T, Etourneau J, Chevalier B et al (2008) Structural, thermal, and electrical properties of CrSi2. J Appl Phys. https://doi.org/10.1063/1.2917347

[13] Goroshko D, Chusovitin E, Bezbabniy D et al (2015) Formation and Thermoelectric Properties of Si/CrSi2/Si (001) Heterostructures with Stressed Chromium Disilicide Nanocrystallites. Electron Mater Lett 11:424–428. https://doi.org/10.1007/s13391-015-4475-5

[14] Nishida I (1972) The crystal growth and thermoelectric properties of chromium disilicide. J Mater Sci 7:1119–1124

[15] Pandey T, Singh AK (2014) Origin of enhanced thermoelectric properties of doped CrSi2. RSC Adv 4:3482–3486. https://doi.org/10.1039/c3ra44822c

[16] Burkov AT, Novikov SV, Khovaylo VV, Schumann J (2017) Energy filtering enhancement of thermoelectric performance of nanocrystalline Cr1-x Six composites. J Alloys Compd 691:89–94. https://doi.org/10.1016/j.jallcom.2016.08.117

[17] Nava F, Tien T, Tu KN (1985) Temperature dependence of semiconducting and structural properties of Cr Si thin films. J Appl Phys 57:2018–2025. https://doi.org/10.1063/1.334389

[18] Caricato AP, Leggieri G, Luches A, Romano F (2007) Morphological and structural characterizations of CrSi2 nanometric films deposited by laser ablation. Appl Surf Sci 254:1224–1227. https://doi.org/10.1016/j.apsusc.2007.09.026

[19] Novikov SV, Burkov AT, Schumann J (2014) Crystallization and Transport Properties of Amorphous Cr-Si Thin Film Thermoelectrics. J Electron Mater 43:2420–2424. https://doi.org/10.1007/s11664-014-3101-x

[20] Kim C (2005) Electrical properties of CrSix, Cr/CrSix/Cr/CrSix, and CrSix/Si/CrSix/Si sputtered on alumina plates. Thin Solid Films 479:182–187. https://doi.org/10.1016/j.tsf.2004.12.019

[21] Novikov SV, Burkov AT, Schumann J (2013) Enhancement of thermoelectric properties in nanocrystalline M – Si thin film composites ( M = Cr, Mn ). J Alloys Compd 557:239–243. https://doi.org/10.1016/j.jallcom.2012.12.088

[22] Park JS, Maeng W-J, Kim H-S, Park J-S (2012) Review of recent developments in amorphous oxide semiconductor thin- fi lm transistor devices. Thin Solid Films 520:1679–1693. https://doi.org/10.1016/j.tsf.2011.07.018

[23] Nili H, Walia S, Balendhran S et al (2014) Nanoscale Resistive Switching in Amorphous Perovskite Oxide (a-SrTiO3) Memristors. Adv Funct Mater 24:6741–6750. https://doi.org/10.1002/adfm.201401278

[24] Ha T, Shin S, Kim HK et al (2013) Use of ordered mesoporous SiO2 as protection against thermal disturbance in phase-change memory. Appl Phys Lett 102:1–4. https://doi.org/10.1063/1.4801476

[25] Schropp REI, Zeman M (1999) New Developments in Amorphous Thin-Film Silicon Solar Cells. IEEE Trans Electron Devices 46:2086–2092

[26] Nolas GS, Goldsmid HJ (2002) Amorphous Thermoelectrics. In: 21st International Conference on Thermoelectrics. pp 296–298

[27] Wu Y, Nyle J, Naseyowma C et al (2009) Comparative Study of the Thermoelectric Properties of Amorphous Zn41Sb59 and Crystalline Zn4Sb3. Chem Mater 21:151–155

[28] Kim S, Kim D, Byeon J et al (2018) Transparent Amorphous Oxide Semiconductor as Excellent Thermoelectric Materials. Coatings. https://doi.org/10.3390/coatings8120462

[29] Sanders IR, Stephen J, Hinder GW et al (2002) The effect of argon implantation on the conductivity of boron implanted silicon. Solid State Electron 20:703–707. https://doi.org/10.1016/0038-1101(77)90047-8

[30] Uzan-Saguy C, Salzman J, Kalish R et al (2002) Electrical isolation of GaN by ion implantation damage: Experiment and model. Appl Phys Lett 74:2441–2443. https://doi.org/10.1063/1.123874

[31] Choudhary R, Chauhan RP (2018) Nitrogen ion implantation effects on the structural, optical and electrical properties of CdSe thin film. J Mater Sci Mater Electron 29:12595–12602. https://doi.org/10.1007/s10854-018-9376-6

[32] Fichtner PFP, Behar M, Kaschny JR et al (2000) Copper gettering at half the projected ion range induced by low-energy channeling He implantation into silicon. Appl Phys Lett 77:972–974. https://doi.org/10.1063/1.1289062

[33] Brett DA, Llewellyn DJ, Ridgway MC (2006) Trapping of Pd, Au, and Cu by implantation-induced nanocavities and

dislocations in Si. Appl Phys Lett. https://doi.org/10.1063/1.2208382

[34] Isoda T, Uematsu M, Itoh KM (2015) Observation of silicon self-diffusion enhanced by the strain originated from end-of-range defects using isotope multilayers. J Appl Phys. https://doi.org/10.1063/1.4931421

[35] Kato M, Arimoto K, Yamanaka J et al (2017) Fabrication of high-quality strain relaxed SiGe(110) films by controlling defects via ion implantation. J Cryst Growth 477:197–200. https://doi.org/10.1016/j.jcrysgro.2017.05.022

[36] Luysberg M, Kirch D, Trinkaus H et al (2002) Effect of helium ion implantation and annealing on the relaxation behavior of pseudomorphic Si1-xGex buffer layers on Si (100) substrates. J Appl Phys 92:4290–4295

[37] Moll A (2018) Elaboration et étude des propriétés thermoélectriques du disiliciure de chrome sous forme de monocristal, de couche mince et de nanofil. Université de Montpellier

[38] Stoller RE, Toloczko MB, Was GS, Certain AG, Dwaraknath FAG (2013) On the use of SRIM for computing radiation damage exposure. Nucl Instr Meth Phys Res B 310:75–80. https://doi.org/10.1016/j.nimb.2013.05.008

[39] Ziegler JF, Biersack JP (2003) Stopping and range of ions in matter: SRIM. http://www.srim.org/

[40] Guen E, Chapuis P-O, Rajkumar R et al (2020) Scanning thermal microscopy on samples of varying effective thermal conductivities and identical flat surfaces. J Appl Phys. https://doi.org/10.1063/5.0020276

[41] Thornton JA (1974) Influence of apparatus geometry and deposition conditions on the structure and topography of thick sputtered coatings. J Vac Sci Technol 11:2–7. https://doi.org/10.1116/1.1312732

[42] Alfonso E, Olaya J, Cubillos G (2012) Thin Film Growth Through Sputtering Technique and Its Applications. In: Andreeta M (ed) Crystallization - Science and Technology. São Paulo

[43] Mayer M (1997) SIMNRA User's Guide. Rep IPP 9/113, Max-Planck-Institut für Plasmaphys Garching, Ger

[44] da Silva DL, Mörschbächer MJ, Fichtner PFP et al (2004) Formation of bubbles and extended defects in He implanted (1 0 0) Si at elevated temperatures. Nucl Inst Methods Phys Res B 219–220:713–717. https://doi.org/10.1016/j.nimb.2004.01.148

[45] Oliviero E, Peripolli S, Amaral L et al (2006) Damage accumulation in neon implanted silicon. J Appl Phys. https://doi.org/10.1063/1.2220644

[46] Oliviero E, Peripolli S, Fichtner PFP, Amaral L (2004) Characterization of neon implantation damage in silicon 112:111–115. https://doi.org/10.1016/j.mseb.2004.05.014

[47] Qiang-Li KW, Schroeder H et al (1990) Gas densities in helium bubbles in nickel measured by small angle neutron scattering. Acta Met Mater 38:2383–2392

[48] Rowe DM (2006) Thermoelectrics Handbook: macro to nano. Taylor & Francis Group, New York

[49] Was GS (2007) Fundamentals of Radiation Materials Science. Springer

[50] Perumal S, Gorsse S, Ail U et al (2013) Effect of co-substitution of Mn and Al on thermoelectric properties of chromium disilicide. J Mater Sci 48:227–231. https://doi.org/10.1007/s10853-012-6732-4

[51] Saji A, Ampili S, Yang SH et al (2005) Effects of doping, electron irradiation, H+ and He+ implantation on the thermoelectric properties of Bi2Se3 single crystals. J Phys Condens Matter 17:2873–2888. https://doi.org/10.1088/0953-8984/17/19/005

[52] Bala M, Bhogra A, Khan SA et al (2017) Enhancement of thermoelectric power of PbTe thin films by Ag ion implantation. J Appl Phys. https://doi.org/10.1063/1.4984050

[53] Banwell TC, Zhao XA, Nicolet MA (1986) Effects of ion irradiation on conductivity of CrSi2 thin films. J Appl Phys 59:3077–3080. https://doi.org/10.1063/1.336931

[54] Desalvo A, Zignani F, Galloni R, Rizzoli R, Ruth M (1993) Doping of amorphous silicon by potassium ion implantation. Philos Mag B 67(1):131–142. https://doi.org/10.1080/13642819308230224

[55] Show Y, Sekine D, Ito H, Izumi T, Iwase M (2000) The Effects of defects on the electrical properties of amorphous carbon layer formed by ion implantation into CVD diamond films. Int J Mod Phys B 14(02n03):218–223. https://doi.org/10.1142/S0217979200000212

[56] Tureson N, Marteau M, Cabioch T et al (2018) Effect of ion-implantation-induced defects and Mg dopants on the thermoelectric properties of ScN. Phys Rev B 98:1–9. https://doi.org/10.1103/physrevb.98.205307

[57] Moll A, Hermet P, Bantignies J et al (2020) Influence of Nanostructuration on the Vibrational, Electronic, and Optical Properties of CrSi2 Thin Films. J Phys Chem C 124:28267–28276. https://doi.org/10.1021/acs.jpcc.0c08740

[58] Novikov SV, Burkov AT (2016) Grain boundary scattering contribution to the thermopower in Cr-Si nanocrystalline films. J Phys Conf Ser. https://doi.org/10.1088/1742-6596/769/1/012069

[59] Adelberg M (1967) Effective Thermal Conductivity and Multilayered Insulation. In: Timmerhaus KD (ed) Advances in Cryogenic Engineering, vol 12. Springer, Boston, pp 252–254

[60] Reza A, Yu H, Mizohata K, Hofmann F (2020) Thermal diffusivity degradation and point defect density in self-ion

implanted tungsten. Acta Mater 193:270–279. https://doi.org/10.1016/j.actamat.2020.03.034

[61] Snyder GJ, Toberer ES (2008) Complex thermoelectric materials. Nat Mater 7:105–114